atmosphere

MDPI

Article

Estimating High-Resolution Latent Heat Flux from Satellite (AVHRR-SST) and Reanalysis Data During Summer in the Tokar Gap, Central Red Sea

Jamaan A. Turki * and Fawaz Madah

Departments of Marine Physics, Faculty of Marine Sciences, King Abdul-Aziz University, P.O. Box 80207, Jeddah 21589, Saudi Arabia; fmaddah@kau.edu.sa
* Correspondence: jturki@kau.edu.sa

Abstract

This study aims to estimate latent heat flux (LHF) over the central Red Sea during the summer months (July and August) of 2000–2020, corresponding with the occurrence of the Tokar Gap (TG) wind jets. Sea surface temperature (SST) was derived from the SeaDAS-based multi-sensor ESA CCI/C3S satellite product (AVHRR-SST), and wind data were obtained from the scatterometer product. Both datasets were re-gridded to a uniform spatial resolution of 0.05°. The AVHRR-SST and scatterometer wind speed were compared with the corresponding ERA5 reanalysis fields. Because both the satellite-derived estimates and ERA5 are model-based products rather than independent in situ observations, this comparison constitutes an intercomparison between two approaches rather than a validation. The AVHRR-SST and scatterometer wind speed showed good agreement with ERA5 fields (correlation coefficients CC = 0.66 and 0.93, respectively). The spatial distribution of the estimated LHF reproduced the ERA5 LHF patterns but with relatively lower magnitudes. Time series analysis near the TG region showed that the estimated LHF underestimated ERA5 values, with a correlation coefficient of 0.77 and a root mean square error (RMSE) of 25.8 W/m^2. The results represent an intercomparison between two model- and satellite-based approaches and are limited by the absence of independent in situ buoy observations for direct validation.

Keywords: central Red Sea; latent heat flux; Tokar Gap; wind jet

1. Introduction

Among the four heat flux components, latent heat flux (LHF) plays a critical role in the transfer of heat and water vapor between the ocean and the atmosphere. Turbulent fluxes, mainly LHF and sensible heat flux (SHF), cannot be measured directly by remote sensing satellites because they depend on several factors that cannot be accurately estimated from space, such as near-surface air specific humidity and air temperature [1]. The era of finer and higher-resolution sea surface temperature (SST) observations started in the early 1980s. One such product is the NOAA Daily Optimum Interpolation SST (DOISST) at 0.25° resolution, which has been available since the early 1980s [2]. More recently, the European Space Agency (ESA) Climate Change Initiative (CCI) [3] has achieved a spatial resolution of 0.05° for SST datasets.

In contrast, reanalysis studies and products have become increasingly important in climate and oceanic research. Their widespread use is partly attributable to the lack of

Academic Editor: Ferdinando Salata

Received: 24 June 2026
Revised: 27 July 2026
Accepted: 27 July 2026
Published: 29 July 2026

 https://doi.org/10.3390/atmos17080738

observational data in some regions as well as the lower cost of reanalysis data compared to observational data, which often require costly maintenance and frequently suffer from significant gaps in the records. Moreover, one of the biggest advantages of reanalysis data is their extensive spatial and temporal coverage and high resolution. Reanalysis data combine several datasets to produce a reliable climate estimate. Although reanalysis data are based on reliable sources, they still need to be calibrated for accuracy.

An increasing number of studies have used remote sensing and reanalysis datasets to estimate air–sea variables, including downward shortwave radiation [4], longwave radiation [5–7], surface net radiation [8–10], and LHF [11,12]. Heat fluxes in the Red Sea (RS) have been examined in many studies [13–18].

Regarding wind gap investigations, the study [19] first described gap winds as a flow pattern that develops when lower atmospheric flow is constrained by higher topographic features. Since then, several studies have examined wind jets in various regions (e.g., [13,18,20–26]).

The RS is a marginal sea formed by tectonic movements and is characterized by high mountain ridges along the basin that control the wind patterns over it [27]. The average depth of the RS is ~500 m, whereas the maximum depth exceeds 2000 m [28] (Figure 1). The RS experiences several cross-axis wind jets due to the varying altitudes of the mountain chains that cover both sides of the basin. These altitude differences drive wind jets from areas of high to low pressure, resulting in the development of wind gap jets [13,24,26]. The Tokar Gap (hereafter TG) is a significant gap located on the East African coast, measuring 110 km wide and 50 km long. In summer, TG wind jets are considered the most prominent jets along the east coast [13], and Pratt et al. [26] have stated that the speed of wind jets from the TG can reach 25 m/s. In summer, the RS has one of the highest silt concentrations in the Northern Hemisphere, resulting from dust storms that cross from the Sahara Desert through the TG into the RS [29]. In contrast, the wind jet system at the mountain gap reverses during winter [30].

The wind pattern in the RS changes seasonally. During summer, the entire basin is affected by the Mediterranean weather system, which generates north-northwest (NNW) winds. In contrast, during winter, the Indian monsoon weather system affects only the southern part of the RS, reversing the wind direction to south-southeast (SSE) [31,32]. This wind regime significantly influences the circulation and water exchange between the RS and the Gulf of Aden [24,32].

The spatial distribution of SST in the RS is shaped by climatic and geographic factors. SST generally increases from north to south. The north–south temperature gradient is most pronounced during summer, when the SST in the southern RS exceeds 31 °C—one of the highest values recorded globally [32]. The RS exhibits a clear seasonal cycle in SST, with peak values occurring in late summer (August and September) and minimum temperatures occurring in winter (January and February) [27]. One study showed that the narrow strait at the southern end of the RS restricts exchange with the open ocean, thereby elevating sea temperatures, particularly in the central and southern regions [33].

Previous studies estimating heat fluxes in the RS have reported varying values over the years, owing to advances in technology and differences in data collection and estimation methods. Primarily, Patzert [31] used voluntary observing ship data and found that the RS gains more heat than it loses. He attributed this net heat gain to the underestimation of LHF or overestimation of longwave radiation. The authors of [34] examined the heat and freshwater budgets using historical data from the Comprehensive Ocean–Atmosphere Data Set (UWM/COADS). Their estimated net heat flux was overestimated by approximately 100 W/m^2, primarily due to underestimation of LHF. Sofianos and Johns [35] used 18-month direct observations at Bab el Mandeb Strait to estimate the heat and freshwater budgets of the RS. Their results showed large differences and uncertainties compared with earlier estimates, which were likely due to the higher accuracy of the in-situ data. Papadopoulos et al. [36] analyzed multiple observational and reanalysis datasets for the northern RS and concluded that LHF and SHF play major roles in the net surface heat exchange.

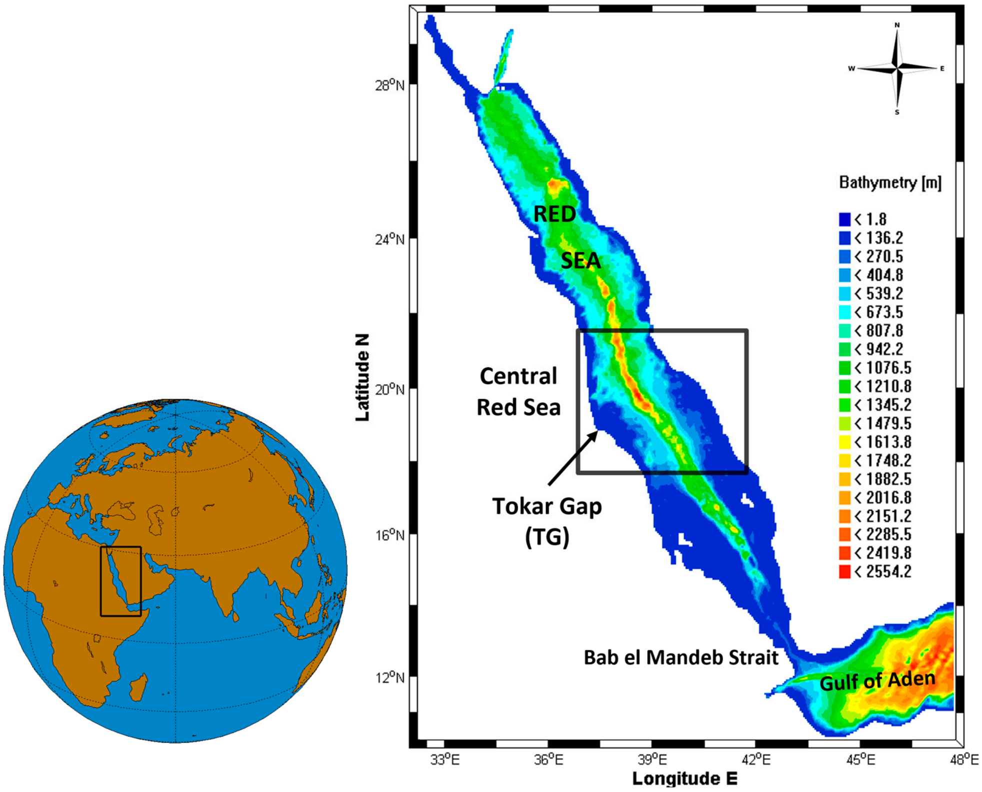

Figure 1. Map of the study area showing the bathymetry. The black square represents the region of the Tokar Gap (TG) wind jets. Inset (**left**): global map showing the location of the Red Sea (black rectangle).

The authors of [37] employed the COARE bulk flux algorithm with data from an air–sea interaction buoy and observed high heat loss during strong wind events, reaching up to 500 W/m^2. The impact of winds on the RS was investigated in [25] using MERRA2 reanalysis data and measurements from a floating buoy. Their results indicated that high wind events cause intense heat loss, leading to the dominance of LHF over the other flux components. The authors of [15] estimated LHF from buoy observations and compared the values with ERA5 and MERRA2 reanalysis datasets. Both reanalysis products showed strong correlations with the buoy data (0.97 for ERA5 and 0.98 for MERRA2).

As noted above, most previous studies have estimated heat fluxes using reanalysis or satellite data with relatively coarse spatial resolution. Therefore, the present study aims to estimate LHF at a finer spatial resolution of 0.05 over a 21-year period (2000–2020). Additionally, the performance of this LHF estimation is evaluated and compared with the ERA5 reanalysis dataset. The remainder of this paper is organized as follows: Section 2 describes the data and methodology, Section 3 presents the results, Section 4 discusses the findings, and Section 5 provides the conclusion.

2. Data and Methods

The study area is the central RS, situated between 16° N and 20° N and 37.50° E to 42.80° E, between the African continent and the Arabian Peninsula. This study is based on the use of atmospheric and oceanic data obtained from several datasets to estimate LHF.

The analysis covers the period 2000 to 2020, focusing only on July and August, when the wind jets occur, as shown in previous investigations [13,18,23].

The Advanced Very High-Resolution Radiometer (AVHRR) and its successor, the Visible Infrared Imaging Radiometer Suite (VIIRS), are limited to measuring spectral reflectance and radiance. Therefore, the variables required to estimate LHF are obtained from three datasets to provide relative humidity, air temperature, surface pressure, shortwave radiation, and longwave radiation. The first dataset comprises SST data from the ESA Climate Change Initiative (CCI)/Copernicus C3S multi-sensor SST product (v2.1), which merges observations from numerous polar-orbiting infrared radiometers, including AVHRR and its successors, using a SeaDAS-based Bayesian cloud-screening and retrieval scheme [3]. This dataset is a comprehensive and ongoing climate data record that begins in 1981, is updated twice daily, and is gap-filled and gridded at 0.05° (~4 km) spatial resolution. It is hereafter referred to as AVHRR-SST.

The second dataset consisted of scatterometer observations (an independent scatterometer wind product) used to obtain surface wind speed, wind stress, zonal wind, and meridional wind components. This product has a spatial resolution of 0.125° per grid cell and an hourly temporal resolution [38] (hereafter referred to as scatterometer wind).

The third dataset used in this study is ERA5, the fifth-generation reanalysis dataset produced by the European Centre for Medium-Range Weather Forecasts (ECMWF) [38]. The dataset has an hourly temporal resolution and a spatial resolution of 0.25°. It covers the period from 1940 to the present and provides improved reanalysis data compared with previous generations. The variables downloaded from ERA5 for this study include air temperature, dew point, cloud cover, rain rate surface pressure, surface downward shortwave radiation, surface downward longwave radiation, and surface upward latent heat flux. All fluxes are provided in Jm^{-2} and were converted to Wm^{-2} using the following equation [39]:

$$Flux\ (\mathrm{Wm}^{-2}) = \frac{Flux\ (\mathrm{Jm}^{-2})}{days\ seconds\ in\ month}$$

The data are available at https://cds.climate.copernicus.eu/ (accessed on 15 January 2026).

Moreover, wind stress data were obtained from scatterometer observations and their collocated European Centre for Medium-Range Weather Forecasts (ECMWF) fields. The dataset has an hourly temporal resolution and a spatial resolution of 0.125°. The variables used in this study include eastward stress, northward stress, wind stress, and wind stress curl.

Data from 21 years were used in this study to estimate LHF from the AVHRR satellite observational dataset for the central RS. The AVHRR data provides two measurements per day, one during the daytime and one during the nighttime. To match this sampling frequency, the ERA5 data were averaged to produce daily values based on these two observations. Therefore, all atmospheric variables of ERA5 used as inputs to the COARE 3.6 algorithm represent the average of the daytime and nighttime overpass times, ensuring temporal consistency with the AVHRR-SST and scatterometer observations. As a result, the monthly LHF estimates represent combined daytime and nighttime conditions rather than a single time of day. Table 1 summarizes the datasets used in this study, including their sources, variables, and spatial and temporal resolutions.

Data pre-processing and analysis were performed using the Climate Data Operator (CDO) software, developed by the Max Planck Institute. CDO is an open-source scientific tool for climate data processing, analysis, and visualization [39]. The hourly data were aggregated into daily values and subsequently averaged to monthly values using CDO. To ensure consistency among the different datasets, bilinear interpolation following the method of Wang et al. [40] was applied to re-grid all datasets to a common spatial resolution of 0.05° (~4 km). In addition, ERA5 wind speed was computed from the zonal and meridional wind components using CDO. It should be noted that the bilinear interpolation of the scatterometer (0.125°) and ERA5 (0.25°) datasets onto the common 0.05° grid represents a spatial re-gridding procedure rather than true dynamic downscaling. Therefore, the effective spatial information content of these datasets remains constrained by their original, coarser resolution.

Table 1. Summary of data sources, variables, and spatial and temporal resolutions used in this study.

Variable(s)	Source Dataset	Spatial Resolution	Temporal Resolution	Reference
SST (AVHRR-SST)	ESA CCI/Copernicus C3S multi-sensor SST product (v2.1)	0.05°	Twice daily	[3]
Wind speed, zonal and meridional wind Wind stress (eastward/northward), wind stress curl	Scatterometer (Copernicus Marine Service)	0.125°	Hourly	[38]
Air temperature, dew point, cloud cover, rain rate, surface pressure, shortwave/longwave radiation LHF (for intercomparison)	ERA5 reanalysis (ECMWF)	0.25°	Hourly	[39]

To estimate LHF values, the Coupled Ocean–Atmosphere Response Experiment (COARE 3.6) was used [41]. This algorithm is widely used and considered one of the most robust and extensively validated methods for estimating air–sea heat fluxes, although its performance can vary depending on the region and atmospheric conditions [9,42]. The algorithm calculates LHF using the following equation, while incorporating corrections for atmospheric stability, skin temperature, and warm layer effects [42]:

$$Q_L = \rho_{air} \; C_e L_e U_z (q_s - q_z) \quad (1)$$

where ρ_{air} is the air density (kg m^{-3}), C_e is the dimensionless turbulent transfer coefficient for latent heat, L_e is the latent heat vaporization (J kg^{-1}), U_z is wind speed (m s^{-1}) at the reference height z, q_z refers to the air value at a reference height, and q_s denotes the surface value.

This method has been widely used to estimate and compare air–sea heat fluxes with reanalysis products (e.g., [9,42]). The COARE 3.6 algorithm requires several input variables, including wind speed, SST, air temperature, specific humidity, relative humidity, shortwave radiation, longwave radiation, cloud cover, and rain rate, to estimate wind stress, LHF, and SHF. Relative humidity is calculated within the COARE3.6 function using the following equation [42]:

$$RH(\%) = 100 \, \frac{e}{e_s}$$

where e is the actual vapor pressure and e_s is the saturation vapor pressure (both reported in mb).

In the RS, the accuracy of ERA5 was validated against independent buoy observations in previous studies (e.g., [15,18]), whereas the AVHRR-SST and scatterometer wind products have yet been evaluated against in situ data in this region, although they have been employed in several studies [43–45]. It is important to note that surface fluxes of ERA5, including LHF, are model-derived estimates generated using a bulk parameterization scheme rather than direct observations. Consequently, the comparison performed between the AVHRR/scatterometer-based estimates and ERA5 represents an intercomparison between two model- and satellite-based approaches, since no independent in situ (buoy) measurements were available for the present study.

To represent a time series for the estimated LHF and ERA5, an areal mean approach was carried out by averaging time series values within a box surrounding the TG region (Figure 1). The resulting monthly time series were then compared with the corresponding ERA5 areal mean values using Pearson's correlation coefficient (CC), root mean square error (RMSE), mean absolute difference (MAD), *p*-value, and the 95% confidence interval of the correlation coefficient.

3. Results

This study aimed to estimate high-resolution LHF using satellite-derived SST (AVHRR-SST) and scatterometer wind observations, both re-gridded to a spatial resolution of 0.05°, for the central RS. The spatial distribution of SST (AVHRR-SST) and wind speed (scatterometer) in the central RS are presented in Figure 2. The SST distribution shows an increase in temperature toward the south (Figure 2). During July and August, the lowest mean SST is observed near the eastern coast of the RS, between 19° and 20.5°, with mean temperature ranging from 29.5 °C to 30.50 °C. Along the western coast, the lowest mean SST is also located between 19° N and 20.5° N, with an average temperature of approximately 30.0 °C. In contrast, the highest mean SST increases toward the southern part of the RS, reaching approximately 31.6 °C.

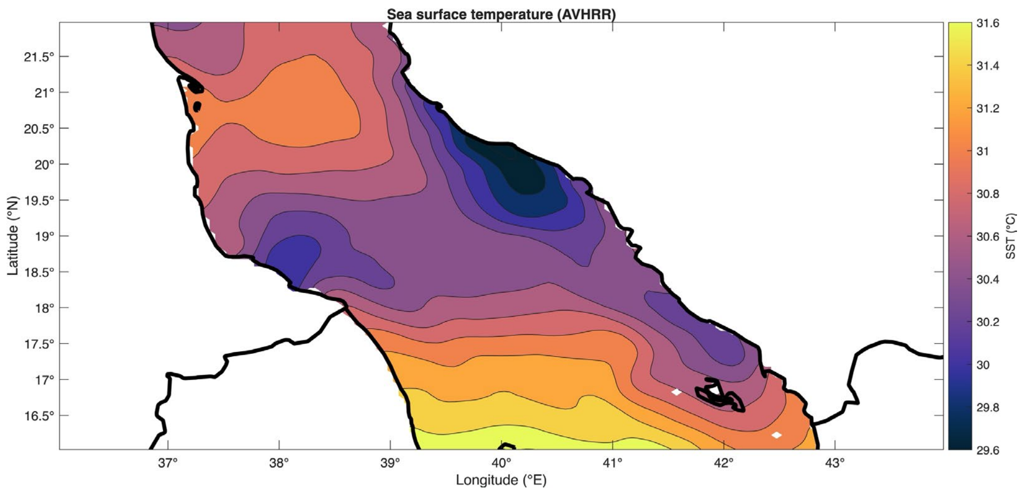

Figure 2. Monthly mean SST spatial patterns derived from AVHRR-SST for July and August during 2000–2020 in the central Red Sea.

The monthly mean wind speed distribution is presented in Figure 3 and shows a distinct zonal wind pattern originating from the TG. The strongest winds emerge from the TG and maintain their high intensity until they reach the central part of the RS. Beyond this region, wind speeds gradually decrease and merge with the prevailing wind pattern over the RS. Figure 4 illustrates the spatial distribution of wind stress curl. Positive wind stress curl indicates the divergence of surface water, which promotes upwelling events, whereas negative wind stress curl causes convergence of surface waters and favors downwelling events. Near the TG, the strong wind jet and the associated positive wind stress curl generate upwelling that can extend toward the eastern coast of the RS.

Because this study focuses on the TG region, an areal-mean box approach was adopted. Therefore, area-averaged time series of SST, wind speed, relative humidity, air temperature, and cloud cover were calculated over the TG region. Figure 5 illustrates the monthly mean time series of satellite-derived variables (AVHRR-SST and scatterometer wind) and ERA5 variables required to estimate LHF in the central RS during July and August from 2000 to 2020. These variables include SST, wind speed, air temperature, relative humidity, shortwave radiation, long wave radiation, and cloud cover.

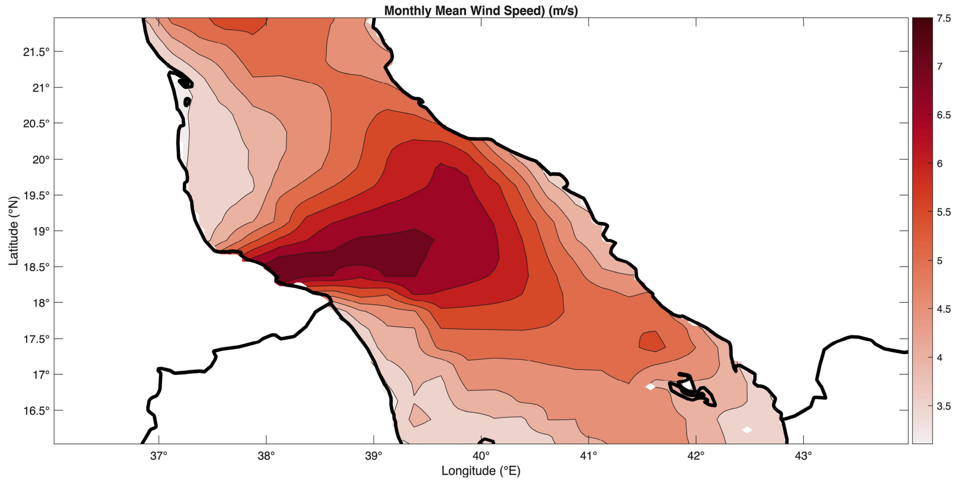

Figure 3. Monthly mean wind speed derived from scatterometer observations for July and August during 2000–2020 in the central Red Sea.

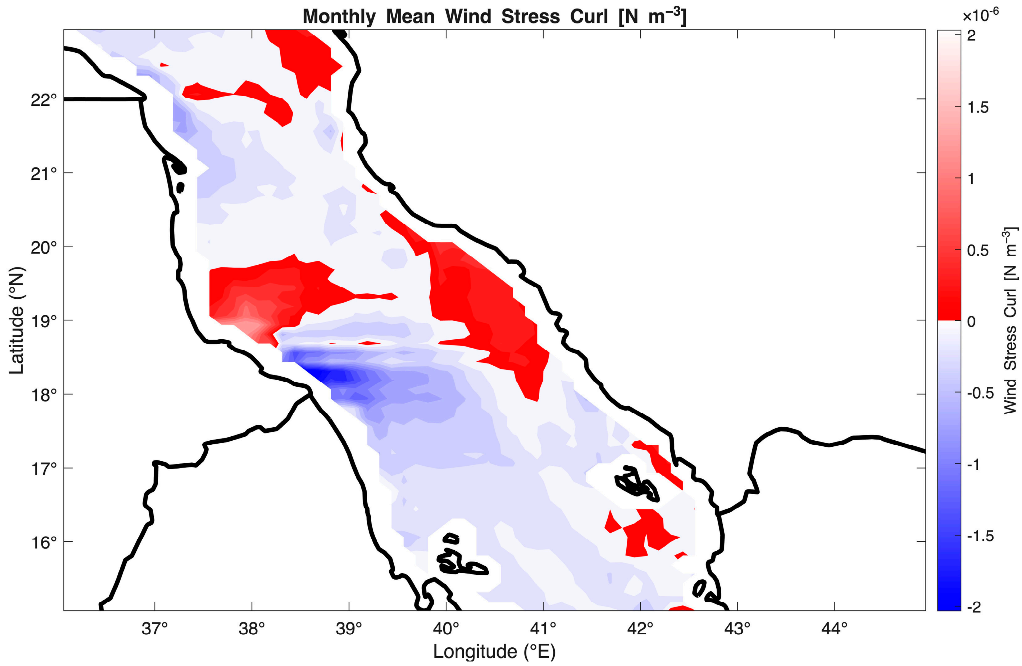

Figure 4. Monthly mean wind stress curl values computed from the collocated scatterometer wind stress product for July and August during 2000–2020 in the central Red Sea.

Table 2 presents the statistical comparison of SST and wind speed from the two datasets to assess their agreement. The SST variability exhibited a similar pattern in both datasets, ranging from 29 °C to 32 °C with mean of 30.32 °C and std value of 0.57 °C (Figure 5a). Following the CC values in Table 2, the AVHRR and ERA5 SST datasets showed strong agreement. The RMSE values for SST and wind speed were 0.46 and 0.53, respectively. In addition, MAD values were within an acceptable range. Table 3 summarizes the statistical characteristics of the variables used to estimate LHF, which are also shown in Figure 5. Air temperature consistently exceeded SST by approximately 1–2 °C at each time point (Figure 5c). The monthly mean wind rose plots for the scatterometer and ERA5 datasets are presented in Figure 6. The dominant wind direction was westerly, representing the TG wind flow from the mountain gap toward the RS. The westerly direction accounted for approximately 43% scatterometer wind observations, compared with approximately 33% for ERA5, although ERA5 showed higher wind speed magnitudes overall.

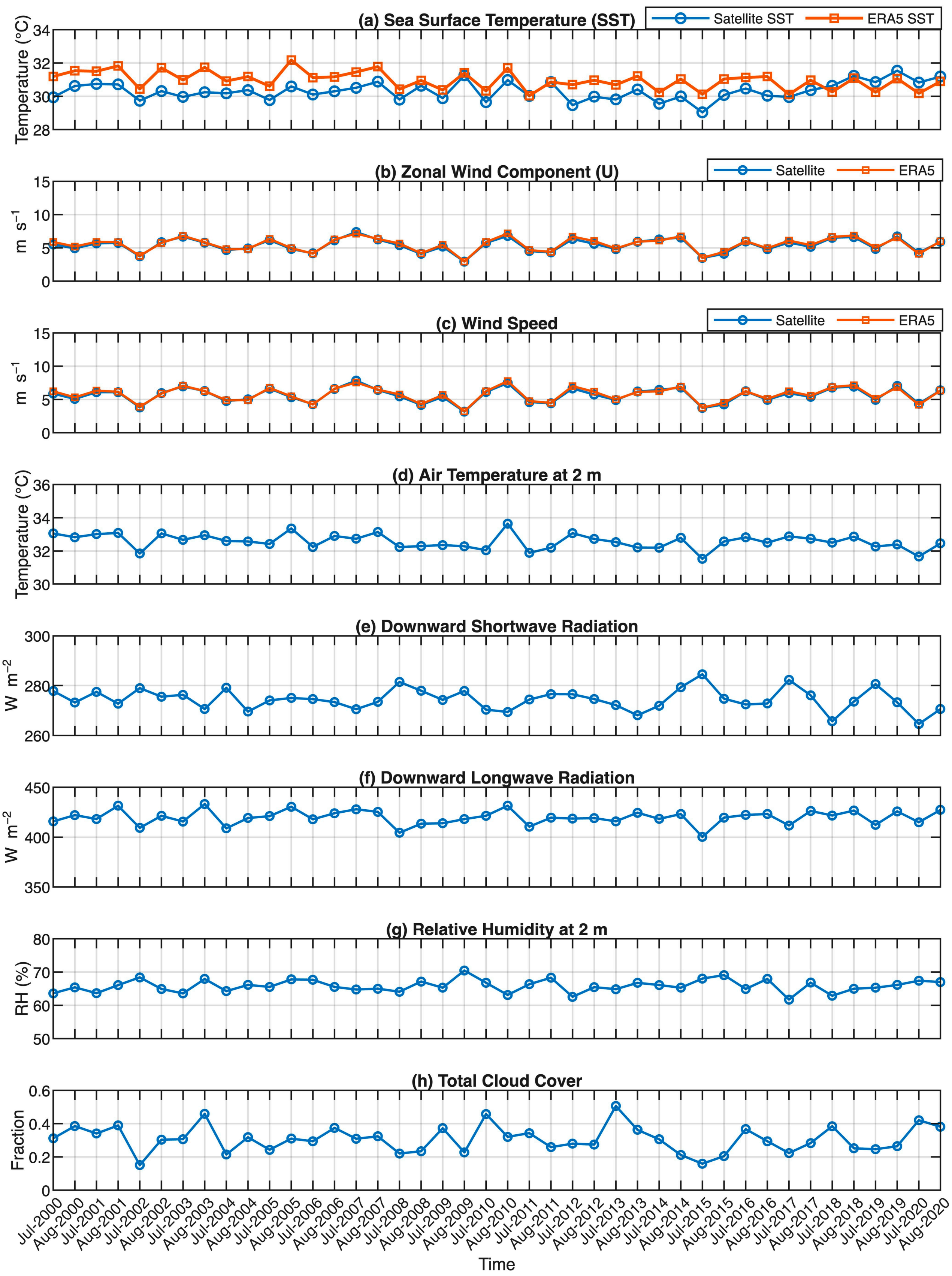

Figure 5. Monthly mean time series of (**a**) SST, (**b**) Zonal wind component (U), (**c**) Wind speed, (**d**) Air temperature at 2 m, (**e**) Downward shortwave radiation, (**f**) Downward longwave radiation, (**g**) Relative humidity, and (**h**) Total cloud cover for the entire period (2000–2020).

Table 2. Statistical comparison of SST (AVHRR-SST vs. ERA5) and wind speed (scatterometer vs. ERA5).

Parameters	CC	RMSE	MAD
SST (°C)	0.66	0.46	0.42
Wind speed (m/s)	0.93	0.53	0.49

Table 3. Summary of the statistical analysis of the monthly mean time series for SST and wind speed (derived from AVHRR-SST and scatterometer observations, respectively) and air temperature, humidity, and cloud cover (ERA5) for the period 2000–2020.

Parameters	Min	Max	Mean	Std
Satellite SST (°C)	29.03	31.54	30.32	0.57
ERA5 SST (°C)	30.03	32.18	30.96	0.54
Satellite zonal wind (m/s)	2.94	7.37	5.41	1.00
ERA5 zonal wind (m/s)	2.95	7.17	5.53	1.02
Satellite wind speed (m/s)	3.17	7.84	5.66	1.09
ERA5 wind speed (m/s)	3.21	7.76	5.75	1.09
Air temp (°C)	31.53	33.65	32.58	0.45
Short wave radiation (W/m^2)	264.58	284.51	274.47	4.22
Long wave radiation (W/m^2)	400.31	433.23	419.71	7.23
Humidity (%)	61.37	70.64	65.83	1.88
Cloud cover (%)	0.15	0.51	0.31	0.08

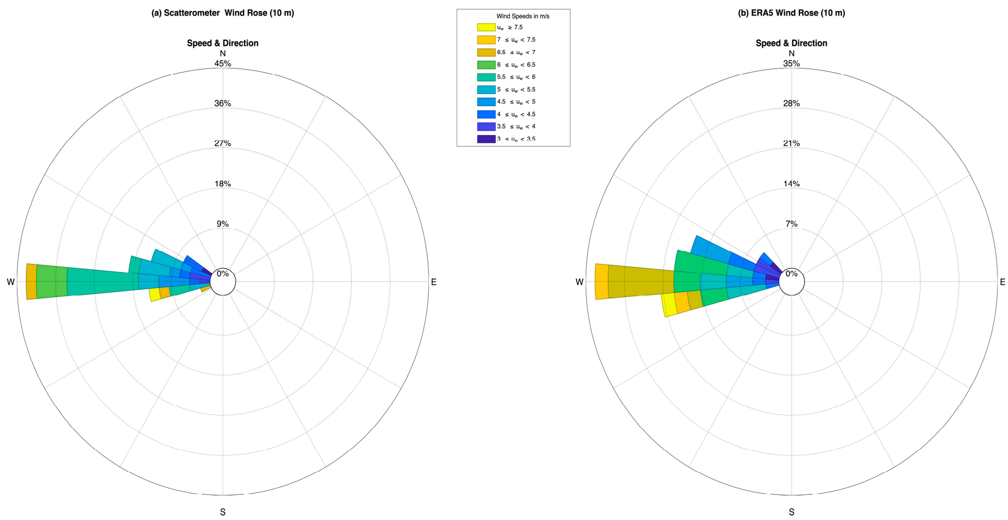

Figure 6. Monthly mean wind roses near the Tokar Gap derived from (**a**) scatterometer observations and (**b**) ERA5 data.

Because this study focuses on estimating LHF and does not include an analysis of other heat flux components, all LHF values are presented as positive, representing evaporation. Figure 7 shows the spatial distribution of the estimated LHF and the ERA5 LHF. The highest estimated LHF values are observed near the TG, between 18.50° N–19° N and 38.20° E–40.50° E (Figure 7a), indicating the influence of the TG wind jets. This is evidenced by the elevated LHF values near the TG coast, which gradually decrease with increasing distance from the region. In contrast, the lowest mean LHF values are observed both north and south the wind jet location, highlighting the influence of the TG wind jets on the spatial distribution of LHF in the central RS. Moreover, the spatial pattern of the ERA5 LHF indicates generally higher monthly mean values than those estimated in this study (Figure 7b). The highest monthly mean LHF values are concentrated near the exit of the TG wind jet. In contrast, except for the TG region and coastal areas, the LHF distribution over the central RS appears relatively homogeneous, with values ranging between 100 and 150 W/m^2.

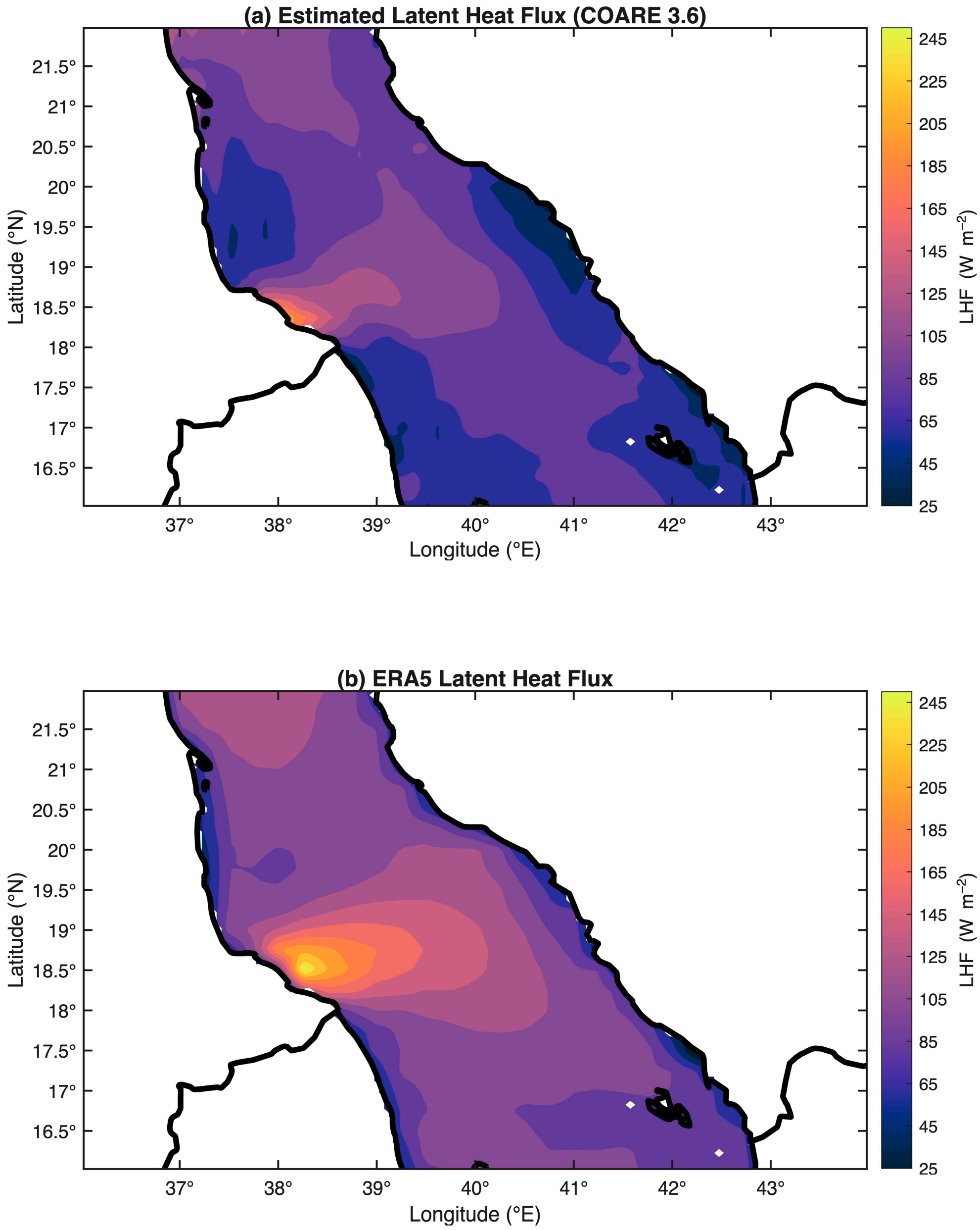

Figure 7. Mean monthly spatial pattern of (**a**) the estimated LHF and (**b**) ERA5 LHF.

Figure 8 illustrates the monthly mean time series of the estimated LHF and ERA5 LHF over the entire period. Both the estimated LHF and ERA5 LHF exhibit similar temporal patterns, although the estimated LHF generally underestimated or overestimated slightly the ERA5 values. The statistical comparison between the monthly estimated LHF and ERA5 LHF is listed in Table 4. The estimated LHF ranged from 73.6 to 272.5 W/m^2, with a mean of 176.1 ± 40.68 W/m^2, while ERA5 LHF ranged from 109.7 to 231.0 W/m^2, with a mean of 173.6 ± 29.4 W/m^2. Both time series showed a strong correlation (CC = 0.77, 95% CI: 0.37–0.87, p = 0.00002). RMSE and MAD were 25.8 and 19.60, respectively, indicating good consistency between the datasets (Table 4). Figure 9 presents the annual time series of estimated LHF and ERA5 LHF over the period 2000–2020. The time series show that both datasets exhibit similar variability, although the estimated values display slightly larger fluctuations in certain years. Statistically, the estimated LHF has a mean of 176.11 ± 34.47 W/m^2 compared to 173.6 ± 24.6 W/m^2 for ERA5, indicating good agreement between the datasets (Table 5). The two series are significantly positively correlated (CC = 0.70, p = 0.0001, 95% CI: 0.39–0.78), with moderate RMSE (24.0 W/m^2) and MAD (18.2 W/m^2).

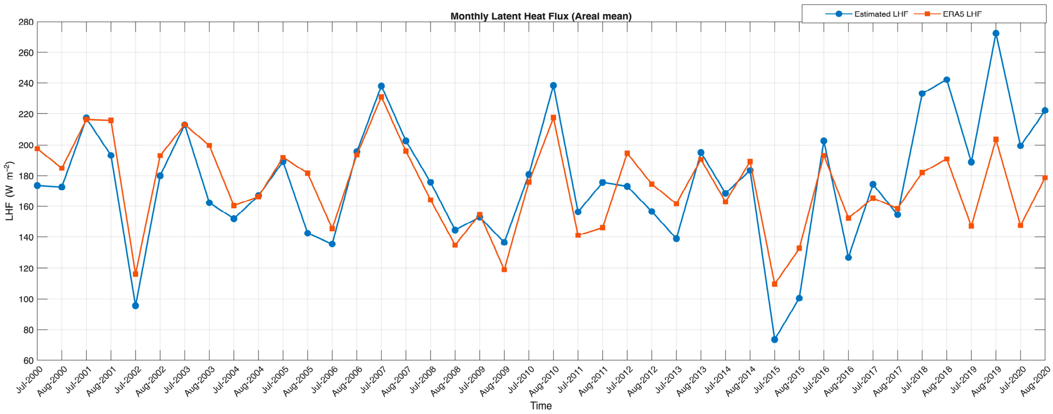

Figure 8. Monthly mean time series for the estimated LHF and ERA5 LHF covering the period from 2000 to 2020.

Table 4. Statistical comparison of monthly estimated LHF and ERA5 LHF.

Parameters	Min	Max	Mean	Std	CC	RMSE	MAD	*p*-Value	Confidence Intervals
Estimated LHF (W/m^2)	73.55	272.47	176.10	40.68	-	-	-	-	-
ERA5 LHF (W/m^2)	109.66	231.00	173.59	29.36	-	-	-	-	-
Estimated LHF (W/m^2) × ERA5 LHF (W/m^2)	-	-	-	-	0.77	25.8	19.6	0.00002	0.37–0.87

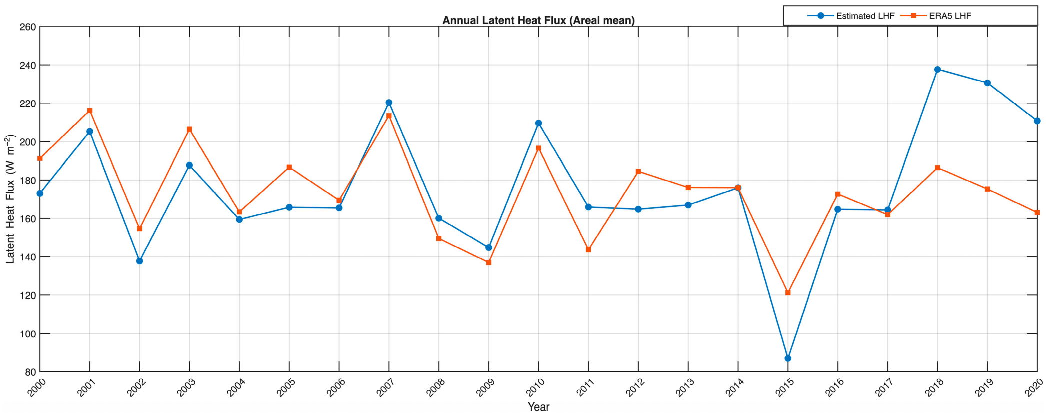

Figure 9. Time series of annual mean estimated LHF and ERA5 LHF covering the period from 2000 to 2020.

Table 5. Statistical comparison of annual estimated LHF and annual ERA5 LHF.

Parameters	Min	Max	Mean	Std	CC	RMSE	MAD	*p*-Value	Confidence Intervals
Estimated LHF (W/m^2)	86.99	237.67	176.11	34.47	-	-	-	-	-
ERA5 LHF (W/m^2)	121.15	216.20	173.59	24.59	-	-	-	-	-
Estimated LHF (W/m^2) × ERA5 LHF (W/m^2)	-	-	-	-	0.70	24.00	18.18	0.0001	0.39–0.78

4. Discussion

The RS is flanked by several mountain gaps along both coastlines, where arid cross-axis wind events occur throughout the year. In the northern part of the RS—mainly along the eastern coastline—LHF is significantly affected by westward wind jets that occur between November and March. Peak values occur in December, ranging from 700 to 900 W/m^2 [13,36,37]. These wind events can trigger surface water mass transformation of the RS overflow due to the high heat loss [13,25,37]. In contrast, TG wind jets coming from the western side of the RS reach their highest mean speed during summer (July and August). These winds significantly increase the wind stress in the area and directly impact the dynamic structure of the basin, which then affects the SST distribution in the central RS. The eastward wind jet from TG can reach a mean monthly speed of 18 m/s [18,23]. Hence, LHF values are significantly influenced by these wind jets, as wind plays a major role in modulating LHF [13,18,46].

The SST pattern in Figure 2 shows an increase in intensity toward the south of the RS, which agrees with the findings of [47]. The lowest SST values are observed in the central RS near TG region and the east coast. This low SST pattern can be related to the wind stress curl in the region induced by TG. The positive wind stress curl patterns in Figure 4 have a similar spatial distribution as the low SST regions shown in Figure 2, suggesting that wind stress curl has a direct effect on SST. This occurs because the wind stress curl in this area causes divergence of surface waters, creating favorable conditions for cold deep water to upwell to the surface. These upwelling events consequently reduce SST values.

Figure 3 shows the monthly mean scatterometer-derived wind speed spatial pattern, which reveals a clear zonal wind extending from the TG to the central RS. Once the wind reaches the central RS, its speed decreases, and its direction shifts to align with the prevailing northerly winds of summer in the region. This wind pattern is consistent with several previous studies that used different datasets (e.g., [13,18,23,26,48]). Figure 4 shows that wind stress curl plays a significant role in driving water circulation and movement within the RS. Positive wind stress curl, associated with the strength of the TG wind jets, promotes upwelling events. The highest values of wind stress curl occur near the gap exit and extend toward the opposite coast of the RS. In contrast, beneath the TG, the interaction between the divergence induced by the TG wind stress curl and the prevailing summer wind pattern generates negative wind stress curl values, favoring downwelling. These upwelling events likely explain the cooler SST observed along the eastern side of the RS as shown in Figure 2 near the TG and the east coast. Our findings are consistent with the recent study by [49].

An areal-mean (i.e., average over a box surrounding the TG region) approach was used to generate time series of several variables. Statistical analysis was then applied to intercompare AVHRR-SST, scatterometer wind, and ERA5. It should be noted that ERA5 surface fluxes are model-based estimates derived from a bulk parameterization scheme; therefore, the agreement reported in this study between the AVHRR/scatterometer-based LHF estimates and ERA5 (CC = 0.77, RMSE = 25.8 W/m^2, MAD = 19.60 W/m^2) reflects an intercomparison between two model- and satellite-based approaches, rather than a true validation against independent observations. A major limitation of this study is the absence of independent in situ or buoy observations, which would be necessary to validate either the satellite-derived or reanalysis-based LHF estimates. In contrast, buoy-based validation studies in the region (e.g., [15]) provide true validation against independent observations. Therefore, the present intercomparison should be interpreted as an assessment of consistency between two different methodologies rather than a confirmation of accuracy. The statistical analysis between SST and wind speed from AVHRR-SST/scatterometer and ERA5 showed acceptable values of correlation, RMSE, and MAD between the two datasets. Moreover, wind rose plot in Figure 5 shows that scatterometer wind data has a higher frequency of winds from the west, the direction from which the TG winds predominantly blow. In contrast, ERA5 wind data exhibits a lower frequency in that direction. Overall, both datasets showed good representation of the wind structure near the TG.

https://doi.org/10.3390/atmos17080738

In general, the air–sea humidity gradient, which is driven mainly by SST-controlled saturation specific humidity at the surface, exerts fundamental physical control on LHF, whereas wind speed modulates its magnitude through the turbulent transfer coefficient (Equation (1)). Together, they act as the main drivers of its variability. Figure 7a illustrates the estimated LHF variability for the central RS. The highest estimated LHF variability was observed near the TG region, which can be attributed to the variability in wind speed associated with the TG.

This mechanism has also been observed in the eastern gaps of the northern RS [15,25,50] and in other studies of the RS region in general [10]. On the other hand, the lowest mean LHF values occur below and above the location of these wind jets from the TG. This low distribution of LHF in the central RS could be attributed to its location beyond the path of the TG. Kumar et al. [51] stated that SST plays a major role in controlling LHF values because it is an essential factor for estimating LHF. Hence, these low LHF values could be affected by the high SST in the region. This relationship was confirmed by Hussein et al. [52], who reported that low wind speeds are primarily responsible for low LHF when SST is high. The interactions among LHF, wind speed, and SST are considered part of an ongoing cycle [53]. Thus, an increase in wind speed can increase LHF rates and decrease the SST. This transition influences wind speed through changes in air pressure which, in turn, affect wind speed and the evaporation rates, as shown in previous studies [54–56].

Overall, high wind speed plays a key role in controlling the LHF distribution in the central RS, as demonstrated by the appearance and impact of the TG wind jets. Figure 7b shows the ERA5 spatial pattern, which exhibits high LHF values in the TG region ranging between 100 and 150 W/m^2. Moreover, except for the TG region and coastal areas, LHF values in the central RS are relatively homogeneous. The estimated monthly mean time series of LHF and the ERA5 reanalysis exhibit similar patterns of LHF variability (Figure 5). However, ERA5 shows higher LHF values than the estimates, with an RMSE of 27 W/m^2 over the entire period. The lower values of the estimated LHF may be attributed to several factors, including differences in the humidity gradient [44], SST, and wind speed between the datasets, as shown in Figure 3. Because all atmospheric inputs to the COARE 3.6 algorithm other than SST and wind speed (air temperature, humidity, radiation, cloud cover) are taken directly from ERA5, part of the agreement between the estimated and ERA5 LHF necessarily reflects these shared input fields. The reported CC may therefore overstate the independent skill attributable to the AVHRR-derived SST and wind speed, and this dependency should be considered.

The estimated LHF differs from the ERA5 LHF mainly because COARE 3.6 accounts for atmospheric stability, surface roughness, wave effects, gustiness, and skin and warm layer temperature corrections. These adjustments play a major role in accurately estimating LHF in a semi-enclosed basin characterized by high SST. In contrast, ERA5 estimates LHF using the bulk formula within its model. However, ERA5 uses skin temperature, which is also the temperature directly measured by AVHRR and is generally lower than bulk SST. Additionally, differences in wind speed between datasets affect the surface humidity gradient, leading to higher LHF estimates in ERA5 compared to the estimated LHF.

5. Conclusions

This study addresses the limited research on Tokar Gap (TG) wind jets and their influence on air–sea interactions in the central Red Sea. LHF was estimated using AVHRR-derived SST and scatterometer wind observations at a high spatial resolution of 0.05°. For this purpose, ERA5 atmospheric variables were re-gridded to a uniform spatial resolution of 0.05° to match the AVHRR grid. The COARE 3.6 bulk flux algorithm was applied using AVHRR-derived SST and wind speed, together with ERA5 atmospheric parameters, including air temperature, shortwave radiation, longwave radiation, cloud cover, and dewpoint temperature. The spatial distribution of the estimated LHF clearly demonstrates the influence of TG wind jets, with high LHF values near the TG coastal region that gradually decrease offshore. Similar spatial patterns were observed in the ERA5 LHF fields, highlighting the important role of strong wind forcing in modifying regional heat exchange processes. Moreover, the estimated monthly mean LHF time series showed temporal variability comparable to that of ERA5, although ERA5 produced higher LHF values (RMSE of 27 W/m^2). These differences could be attributed to the relatively lower SST and wind speed values derived from AVHRR compared with ERA5. In general, the results of this study demonstrate that high-resolution satellite-derived datasets can effectively characterize the air–sea heat flux variability associated with regional wind jet systems in the RS.

Author Contributions: The authors of this study contributed as follows: J.A.T. was responsible for Conceptualization, Data Curation, Formal Analysis, Investigation, Methodology, Software, Validation, Visualization, Writing—Original Draft, and Writing—Review & Editing. F.M. contributed to Supervision, Review and Editing, Validation, and Visualization. All authors have read and agreed to the published version of the manuscript.

Funding: The project was funded by KAU Endowment (WAQF) at king Abdulaziz University, Jeddah, Saudi Arabia. The authors, therefore, acknowledge with thanks WAQF and the Deanship of Scientific Research (DSR) for technical and financial support.

Institutional Review Board Statement: Not applicable.

Informed Consent Statement: Not applicable.

Data Availability Statement: The ERA5 reanalysis data are publicly available from the Copernicus Climate Data Store (https://cds.climate.copernicus.eu/) (accessed on 15 January 2026). The AVHRR-SST data (ESA CCI/C3S SST product) are available from the Copernicus Climate Data Store (https://cds.climate.copernicus.eu/cdsapp#!/dataset/satellite-sea-surface-temperature) (accessed on 20 February 2026). The scatterometer wind data are available from the Copernicus Marine Service (https://data.marine.copernicus.eu/product/WIND_GLO_PHY_L4_NRT_012_004/description) (accessed on 20 February 2026). Derived data products and analysis code supporting the findings of this study are available from the corresponding author upon request.

Acknowledgments: The authors thank the Copernicus Climate Change Service for generating and making the ERA5 data publicly available. Additionally, we sincerely appreciate the Advanced Very High-Resolution Radiometer (AVHRR) Data Centre for making available the data used in this study. During the peer-review process, the authors used Claude (Anthropic) solely to assist in interpreting the reviewers' comments and suggesting possible approaches for addressing them. No artificial intelligence tools were used in the design of the study, preparation of the original manuscript, data analysis, interpretation of the results, or generation of the scientific content. All scientific decisions, manuscript revisions, and final content were made, verified, and approved by the authors.

Conflicts of Interest: The authors declare no conflicts of interest.

References

1. Bourras, D. Comparison of five satellite-derived latent heat flux products to moored buoy data. *J. Clim.* **2006**, *19*, 6291–6313. [CrossRef]
2. Reynolds, R.W.; Smith, T.M.; Liu, C.; Chelton, D.B.; Casey, K.S.; Schlax, M.G. Daily high-resolution-blended analyses for sea surface temperature. *J. Clim.* **2007**, *20*, 5473–5496. [CrossRef]
3. Merchant, C.J.; Embury, O.; Bulgin, C.E.; Block, T.; Corlett, G.K.; Fiedler, E.; Donlon, C. Satellite-based time-series of sea-surface temperature since 1981 for climate applications. *Sci. Data* **2019**, *6*, 223. [CrossRef] [PubMed]
4. Zhang, X.; Liang, S.; Zhou, G.; Wu, H.; Zhao, X. Generating Global LAnd Surface Satellite incident shortwave radiation and photosynthetically active radiation products from multiple satellite data. *Remote Sens. Environ.* **2014**, *152*, 318–332. [CrossRef]

5. Yang, F.; Cheng, J. A framework for estimating cloudy sky surface downward longwave radiation from the derived active and passive cloud property parameters. *Remote Sens. Environ.* **2020**, *248*, 111972. [CrossRef]
6. Wang, T.; Yan, G.; Chen, L. Consistent retrieval methods to estimate land surface shortwave and longwave radiative flux components under clear-sky conditions. *Remote Sens. Environ.* **2012**, *124*, 61–71. [CrossRef]
7. Zhou, Y.; Kratz, D.P.; Wilber, A.C.; Gupta, S.K.; Cess, R.D. An improved algorithm for retrieving surface downwelling longwave radiation from satellite measurements. *J. Geophys. Res. Atmos.* **2007**, *112*, D15. [CrossRef]
8. Xu, J.; Jiang, B.; Liang, S.; Li, X.; Wang, Y.; Peng, J.; Li, S. Generating a high-resolution time-series ocean surface net radiation product by downscaling j-ofuro3. *IEEE Trans. Geosci. Remote Sens.* **2020**, *59*, 2794–2809. [CrossRef]
9. Jiang, B.; Zhang, Y.; Liang, S.; Wohlfahrt, G.; Arain, A.; Cescatti, A.; Zhang, X. Empirical estimation of daytime net radiation from shortwave radiation and ancillary information. *Agric. For. Meteorol.* **2015**, *211*, 23–36. [CrossRef]
10. Jiang, B.; Liang, S.; Ma, H.; Zhang, X.; Xiao, Z.; Zhao, X.; Jia, A. GLASS daytime all-wave net radiation product: Algorithm development and preliminary validation. *Remote Sens.* **2016**, *8*, 222. [CrossRef]
11. Yao, Y.; Liang, S.; Cheng, J.; Liu, S.; Fisher, J.B.; Zhang, X.; Zhao, S. MODIS-driven estimation of terrestrial latent heat flux in China based on a modified Priestley–Taylor algorithm. *Agric. For. Meteorol.* **2013**, *171*, 187–202. [CrossRef]
12. Yao, Y.; Liang, S.; Li, X.; Hong, Y.; Fisher, J.B.; Zhang, N.; Feng, F. Bayesian multimodel estimation of global terrestrial latent heat flux from eddy covariance, meteorological, and satellite observations. *J. Geophys. Res. Atmos.* **2014**, *119*, 4521–4545. [CrossRef]
13. Jiang, H.; Farrar, J.T.; Beardsley, R.C.; Chen, R.; Chen, C. Zonal surface wind jets across the Red Sea due to mountain gap forcing along both sides of the Red Sea. *Geophys. Res. Lett.* **2009**, *36*, L19605. [CrossRef]
14. Zhai, P.; Pratt, L.J.; Bower, A. On the Crossover of Boundary Currents in an Idealized Model of the Red Sea. *J. Phys. Oceanogr.* **2015**, *45*, 1410–1425. [CrossRef]
15. Al Senafi, F.A.; Anis, A.; Menezes, V. Surface Heat Fluxes over the Northern Arabian Gulf and the Northern Red Sea: Evaluation of ECMWF-ERA5 and NASA- MERRA2 Reanalyses. *Atmosphere* **2019**, *10*, 504. [CrossRef]
16. Nagy, H.; Mohamed, B.; Ibrahim, O. Variability of Heat and Water Fluxes in the Red Sea Using ERA5 Data (1981–2020). *J. Mar. Sci. Eng.* **2021**, *9*, 1276. [CrossRef]
17. Mohamed, B.; Nagy, H.; Ibrahim, O. Spatiotemporal Variability and Trends of Marine Heat Waves in the Red Sea over 38 Years. *J. Mar. Sci. Eng.* **2021**, *9*, 842. [CrossRef]
18. Turki, J.A.; Al-Subhi, A.M.; Madah, F. Influence of Tokar Gap wind jet on latent heat flux of Central Red Sea: Empirical orthogonal function approach. *Ocean. Coast. Res.* **2023**, *71*, e23029. [CrossRef]
19. Reed, T.R. Gap winds of the Strait of Juan de Fuca. *Mon. Weather. Rev.* **1931**, *59*, 373–376. [CrossRef]
20. Sharp, J.; Mass, C.F. Columbia Gorge Gap Winds: Their Climatological Influence and Synoptic Evolution. *Weather. Forecast.* **2004**, *19*, 970–992. [CrossRef]
21. Rypina, I.I.; Pratt, L.J.; Pullen, J.; Levin, J.; Gordon, A.L. Chaotic Advection in an Archipelago. *J. Phys. Oceanogr.* **2010**, *40*, 1988–2006. [CrossRef]
22. Smith, D.K.; Li, X.; Keiser, K.; Flynn, S. Regional Air-Sea Interactions (RASI) Climatology for Central America Coastal Gap Wind and Upwelling Events. In *Proceedings of the 2014 Oceans-St. John's*; IEEE: New York, NY, USA, 2015. [CrossRef]
23. Zhai, P.; Bower, A. The response of the Red Sea to a strong wind jet near the Tokar Gap in summer. *J. Geophys. Res. Oceans* **2013**, *118*, 421–434. [CrossRef]
24. Langodan, S.; Cavaleri, L.; Vishwanadhapalli, Y.; Pomaro, A.; Bertotti, L.; Hoteit, I. The climatology of the Red Sea-part 1: The wind. *Int. J. Climatol.* **2017**, *37*, 4509–4517. [CrossRef]
25. Menezes, V.V.; Farrar, J.T.; Bower, A.S. Evaporative implications of dry-air outbreaks over the northern Red Sea. *J. Geophys. Res. Atmos.* **2019**, *124*, 4829–4861. [CrossRef]
26. Pratt, L.J.; Albright, E.J.; Rypina, I.; Jiang, H. Eulerian and Lagrangian Comparison of Wind Jets in the Tokar Gap Region. *Fluids* **2020**, *5*, 193. [CrossRef]
27. Langodan, S.; Cavaleri, L.; Viswanadhapalli, Y.; Hoteit, I. The Red Sea: A Natural Laboratory for Wind and Wave Modeling. *J. Phys. Oceanogr.* **2016**, *44*, 3139–3159. [CrossRef]
28. Morcos, S.A. Physical and chemical oceanography of the Red Sea. *Oceanogr. Mar. Biol. Annu. Rev.* **1970**, *8*, 73–202.
29. Hickey, B.; Goudie, A.S. The use of TOMS and MODIS to identify dust storm source areas: The Tokar Delta (Sudan) and the Seistan Basin (south west Asia). *Geomorphol. Var.* **2007**, *42*, 37–57.
30. Pedgley, D.E. An outline of the weather and climate of the Red Sea. *L'oceanographie Phys. Mer Rouge* **1974**, *11*, 9–27.
31. Patzert, W.C. Wind-induced reversal in Red Sea circulation. *Deep. Sea Res. Oceanogr. Abstr.* **1974**, *21*, 109–121. [CrossRef]
32. Madah, F.; Alsaafani, M. Simulation of 3D Summer Circulation in the Red Sea. *J. Mar. Sci. Eng.* **2025**, *13*, 470. [CrossRef]
33. Cantin, N.E.; Cohen, A.L.; Karnauskas, K.B.; Tarrant, A.M.; McCorkle, D.C. Ocean warming slows coral growth in the central Red Sea. *Science* **2010**, *329*, 322–325. [CrossRef] [PubMed]
34. Tragou, E.; Garrett, C.; Outerbridge, R.; Gilman, C. The heat and freshwater budgets of the Red Sea. *J. Phys. Oceanogr.* **1999**, *29*, 2504–2522. [CrossRef]

35. Sofianos, S.S.; Johns, W.E. An oceanic general circulation model (OGCM) investigation of the Red Sea circulation, 1. Exchange between the Red Sea and the Indian Ocean. *J. Geophys. Res. Oceans* **2002**, *107*, 17-1–17-11. [CrossRef]
36. Papadopoulos, V.P.; Abualnaja, Y.; Josey, S.A.; Bower, A.; Raitsos, D.E.; Kontoyiannis, H.; Hoteit, I. Atmospheric Forcing of the Winter Air–Sea Heat Fluxes over the Northern Red Sea. *J. Clim.* **2013**, *26*, 1685–1701. [CrossRef]
37. Bower, A.S.; Farrar, J.T. Air–Sea Interaction and Horizontal Circulation in the Red Sea. In *Proceedings of the: The Red Sea*; Springer: Berlin, Heidelberg, Germany, 2015; pp. 329–342. [CrossRef]
38. E.U. Copernicus Marine Service Information (CMEMS). *Global Ocean Hourly Sea Surface Wind and Stress from Scatterometer and Model (Product WIND_GLO_PHY_L4_NRT_012_004)*; E.U. Copernicus Marine Service Information (CMEMS): Toulouse, France, 2024. [CrossRef]
39. Hersbach, H. The ERA5 Atmospheric Reanalysis. In *Proceedings of the AGU Fall Meeting*; AGU: New Orleans, LA, USA, 2016; p. NG33D–01.
40. Schulzweida, U. *CDO user guide, 2.3.0*; Zenodo: Geneva, Switzerland, 2023.
41. Wang, T.; Hamann, A.; Spittlehouse, D.L.; Murdock, T.Q. ClimateWNA-High-resolution spatial climate data for western North America. *J. Appl. Meteorol. Climatol.* **2012**, *51*, 16–29. [CrossRef]
42. Fairall, C.W.; Bradley, E.F.; Hare, J.E.; Grachev, A.A.; Edson, J.B. Bulk Parameterization of Air–Sea Fluxes: Updates and Verification for the COARE Algorithm. *J. Clim.* **2003**, *16*, 571–591. [CrossRef]
43. Urraca, R.; Huld, T.; Gracia-Amillo, A.; Martinez-de-Pison, F.J.; Kaspar, F.; Sanz-Garcia, A. Evaluation of global horizontal irradiance estimates from ERA5 and COSMO-REA6 reanalyses using ground and satellite-based data. *Sol. Energy* **2018**, *164*, 339–354. [CrossRef]
44. Raitsos, D.E.; Hoteit, I.; Prihartato, P.K.; Chronis, T.; Triantafyllou, G.; Abualnaja, Y. Abrupt warming of the Red Sea. *Geophys. Res. Lett.* **2011**, *38*, L14601. [CrossRef]
45. Al-Subhi, A.M. Estimation of evaporation rates in the southern Red Sea based on the AVHRR sea surface temperature data. *J. King Abdulaziz Univ. Mar. Sci.* **2012**, *23*, 77–89. [CrossRef]
46. Al-Subhi, A.M.; Taqi, A.M. Surface circulation of the southern red sea as inferred from AVHRR data. *J. King Abdulaziz Univ.* **2014**, *25*, 121. [CrossRef]
47. Davis, S.R.; Pratt, L.J.; Jiang, H. The Tokar Gap jet: Regional circulation, diurnal variability, and moisture transport based on numerical simulations. *J. Clim.* **2015**, *28*, 5885–5907. [CrossRef]
48. Chaidez, V.; Dreano, D.; Agusti, S.; Duarte, C.M.; Hoteit, I. Decadal trends in Red Sea maximum surface temperature. *Sci. Rep.* **2017**, *7*, 8144. [CrossRef] [PubMed]
49. Nicholls, J.F.; Toumi, R.; Stenchikov, G. Effects of unsteady mountain-gap winds on eddies in the Red Sea. *Atmos. Sci. Lett.* **2015**, *16*, 279–284. [CrossRef]
50. El Kenawy, A.M.; Bordbar, M.H.; Mohamed, E.K.; Abdelaal, M.M.; Fernandez-Duque, B.; McCabe, M.F.; Aboelkhair, H. Red Sea warming and its links to the Red Sea dipole and upwelling mechanisms. *J. Mar. Syst.* **2025**, *249*, 104066. [CrossRef]
51. Abualnaja, Y.; Papadopoulos, V.P.; Josey, S.A.; Hoteit, I.; Kontoyiannis, H.; Raitsos, D.E. Impacts of climate modes on air–sea heat exchange in the Red Sea. *J. Clim.* **2015**, *28*, 2665–2681. [CrossRef]
52. Kumar, B.P.; Cronin, M.F.; Joseph, S.; Ravichandran, M.; Sureshkumar, N. Latent heat flux sensitivity to sea surface temperature: Regional perspectives. *J. Clim.* **2017**, *30*, 129–143. [CrossRef]
53. Hussein, M.M. Relationship Between Latent Heat Flux and Sea Surface Temperature in Alexandria Eastern Harbor, Egypt. *Turk. J. Fish. Aquat. Sci.* **2022**, *22*, TRJFAS20642. [CrossRef]
54. Wang, C.; Weisberg, R.H.; Yang, H. Effects of the wind speed–evaporation–SST feedback on the El Niño–Southern Oscillation. *J. Atmos. Sci.* **1999**, *56*, 1391–1403. [CrossRef]
55. Yu, L.; Jin, X.; Weller, R.A. Annual, seasonal, and interannual variability of air–sea heat fluxes in the Indian Ocean. *J. Clim.* **2007**, *20*, 3190–3209. [CrossRef]
56. Weihs, R.R.; Bourassa, M.A. Modeled diurnally varying sea surface temperatures and their influence on surface heat fluxes. *J. Geophys. Res. Oceans* **2014**, *119*, 4101–4123. [CrossRef]